Effects of Temporal Pulse Shaping on Cracking Susceptibility of 6061-T6 Aluminum Nd:YAG Laser Welds

Use of temporal pulse shaping may make it possible to laser weld 6061-T6 aluminum hermetic packages without the need for filler material

BY J. ZHANG, D. C. WECKMAN, AND Y. ZHOU

ABSTRACT. Pulsed laser beam welds of 6061-T6 aluminum alloy hermetic packages for encapsulation of sensitive electronic and optoelectronic components typically exhibit severe solidification cracking when a conventional rectangular or on/off laser pulse is employed. In this study, the effects of temporal pulse shaping on the solidification cracking susceptibility of Nd:YAG pulsed laser welds made in 6061-T6 aluminum were investigated. The results showed that it was possible to eliminate solidification cracking in 6061-T6 pulsed Nd:YAG laser seam welds by decreasing the ramp-down gradient of the laser pulse power after the main welding pulse sector. Crack-free welds were produced over a limited range of trailing ramp-down gradients; however, intermittent solidification cracking recurred when the gradient was further decreased. The solidification cracking susceptibility was also found to increase with increasing peak power density of the main welding sector. Use of a trailing ramp-down pulse shape was found to affect the solidification morphology of the welds. The width of the initial planar grain growth layer at the fusion boundaries and the dendrite and cell spacing increased with decreasing ramp-down gradient. EDS measurements of the overall chemical composition of the solidification crack surfaces of welds showed that microsegregation of Mg, Si, Fe, and Cu to the grain boundaries increased with decreasing ramp-down gradients. This was thought to be the reason for the return of intermittent cracking when low ramp-down gradients were used.

J. ZHANG was with the University of Waterloo. He is now director, Welding Technology Center, Lincoln Electric, China. D. C. WECKMAN and Y. ZHOU are with Department of Mechanical and Mechatronics Engineering, University of Waterloo, Waterloo, Ont., Canada.

Introduction

Encapsulation of electronic and optoelectronic components or assemblies in hermetic enclosures or packages is performed to improve the reliability of these components by providing mechanical support, shielding from electromagnetic interference, better thermal management, and environmental protection of the environmentally sensitive components (Refs. 1, 2). Hermetically sealed electronic packages are widely used in the electronics, communications, automotive, computer, and medical industries. Figure 1 shows an example of an electronic package consisting of a box machined from 6061-T6 aluminum and a 4047 aluminum alloy sheet lid. Once the electronic circuits are assembled into the box, the package is placed in a glove-box environment with the desired enclosure gas and the lid is welded to the box. Wrought aluminum alloys such as 6061-T6 are widely used for microwave amplifier and optoelectronic packages because they are lightweight, and have high corrosion resistance, good workability and machinability, and high thermal and electrical conductivity (Ref. 3).

KEYWORDS

Cracking
Aluminum Alloys
Nd:YAG Laser
Laser Beam Welding
Temporal Pulse Shaping

The quality and durability of the hermetic seal in these packages must be high as failure of the seal can lead to corrosion of the package contents and premature failure of the device (Ref. 4). Pulsed Nd:YAG laser welding has become the method of choice for hermetic sealing of the most critical devices, because it has low and precise heat input that produces a small heat-affected zone, low distortion and residual stresses, is a noncontact process with an ability to weld a wide range of materials, has good process flexibility for automation, and is capable of making reproducible, high-quality welds (Refs. 4–7).

Many wrought aluminum alloys, especially 6xxx series aluminum alloys, are known to be susceptible to hot cracking during fusion welding due to their relatively high thermal expansion coefficient, large solidification shrinkage, and wide solidification temperature range (Refs. 8–16). There are generally two main categories of cracks generated during welding of such aluminum alloys; either solidification cracking within the weld fusion zone or liquation cracking in the partially melted zone (PMZ) adjacent to the fusion boundary (Refs. 8–19). Figure 2 shows an example of a pulsed Nd:YAG laser seam weld made in 6061-T6 aluminum using a series of overlapping on/off or rectangularly shaped laser pulses. This weld has severe solidification cracking (Fig. 2A, B) and also liquation cracking in the PMZ (Fig. 2B) and would, therefore, be unacceptable for electronic packaging or any other applications.

For solidification cracking to occur,

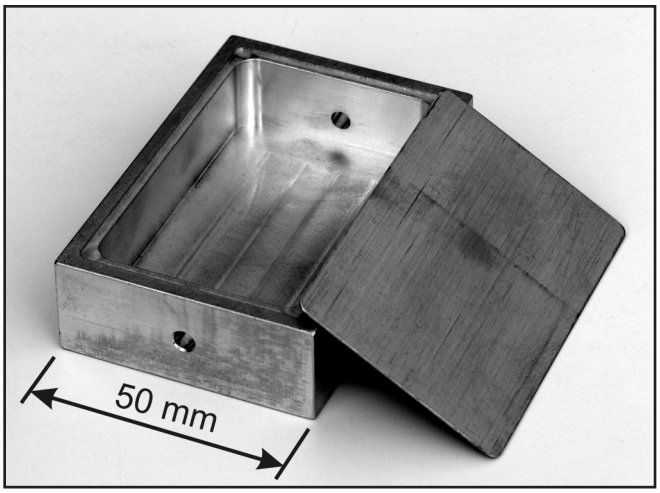

Fig. 1 — Example of an electronic package consisting of a 6061-T6 aluminum machined box and 4047 aluminum sheet lid.

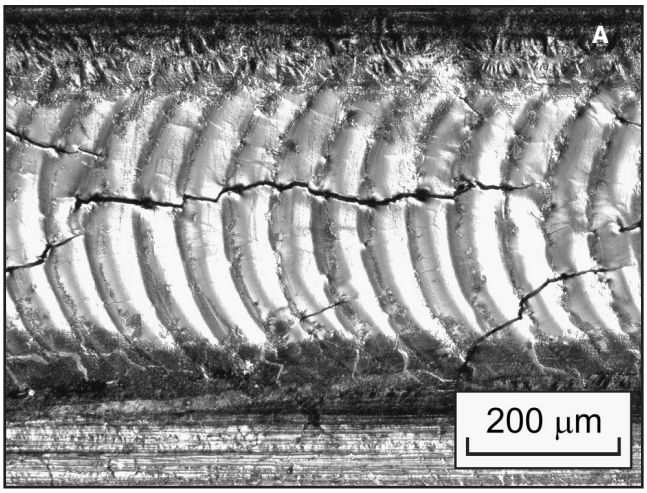

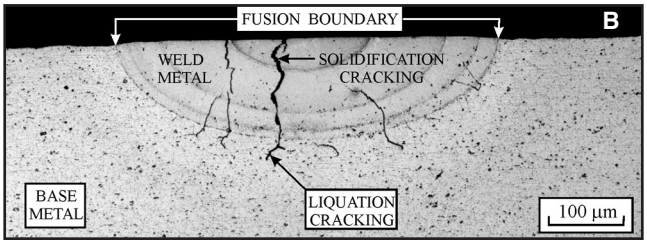

Fig. 2 — Cracks in 6061-T6 aluminum pulsed Nd:YAG laser seam weld. A — Top weld bead showing overlapping spot welds and solidification cracks; B — transverse section solidification and liquation cracks.

two conditions must exist at the solid-liquid interface of the solidifying alloy: one is related to the thermomechanical conditions present and the other is the solidification morphology. Solidification cracking will occur when tensile thermomechanical strains in the material due to thermal contraction of the recently solidified metal causes adjacent dendrites or cellular-dendrites to pull away from each other near the base of the dendrites (Refs. 9, 20, 21). If the distance between the tip and base of the dendrite is large and there is significant restriction to fluid flow down the relatively long narrow passage between the dendrites, then a void will form at the base of the dendrites. Continued solidification will cause growth of this void in the direction of solidification and the creation of a solidification crack similar to those shown in Fig. 2.

The susceptibility of alloys to solidification cracking is influenced by the weld metal composition, the welding process and weld process parameters used, and the restraint to thermal contraction due to weldment and joint design or clamping. For example, solidification cracking susceptibility is known to increase with alloy freezing range, which in turn is influenced directly by the alloy composition, the presence of impurities, and microsegregation due to nonequilibrium solidification effects (Refs. 8, 9, 18–21). A longer freezing range will promote the formation of long, thin dendritic morphology with poor fluid flow between the dendrites. Cracking susceptibility is also influenced by the solidification microstructure, the amount and distribution of liquid at the final stage of solidification, the primary solidification phase, the surface tension of the grain boundary liquid, the grain structure, and the ductility of the solidifying weld metal (Refs. 17–21). For a given alloy composition, the dendrite spacing, nonequilibrium freezing range, and the distance from start to finish of solidification are all affected by the local growth velocity and temperature gradient (Refs. 20, 21). All of these factors affect the resistance to fluid flow between the dendrites and, therefore, influence cracking susceptibility.

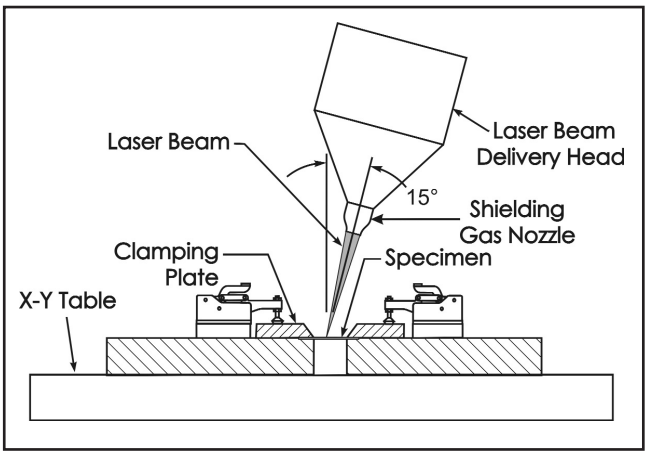

Fig. 3 — Schematic diagram of the welding jig and Nd:YAG laser beam delivery head.

Several techniques have been reported to be effective in reducing or eliminating solidification cracking in laser welded aluminum alloys. The first approach involves use of a filler metal with a different composition and shorter freezing range. Normally, 4xxx and 5xxx series welding wires or Al-Si alloy foil can be used to move the weld metal composition and freezing range away from the crack-sensitive range (Refs. 8, 9, 14, 15, 22, 23). When fabricating hermetic packages by laser welding, this can be also be done by making the lid

Table 1 — The Nominal Composition (wt-%) of AA6061-T6 Aluminum (Ref. 32)

Mg	Si	Cr	Fe	Cu	Mn	Zn	Ti	Al
0.8–1.2	0.4–0.8	0.04–0.35	0.7	0.15–0.40	0.15	0.25	0.15	balance

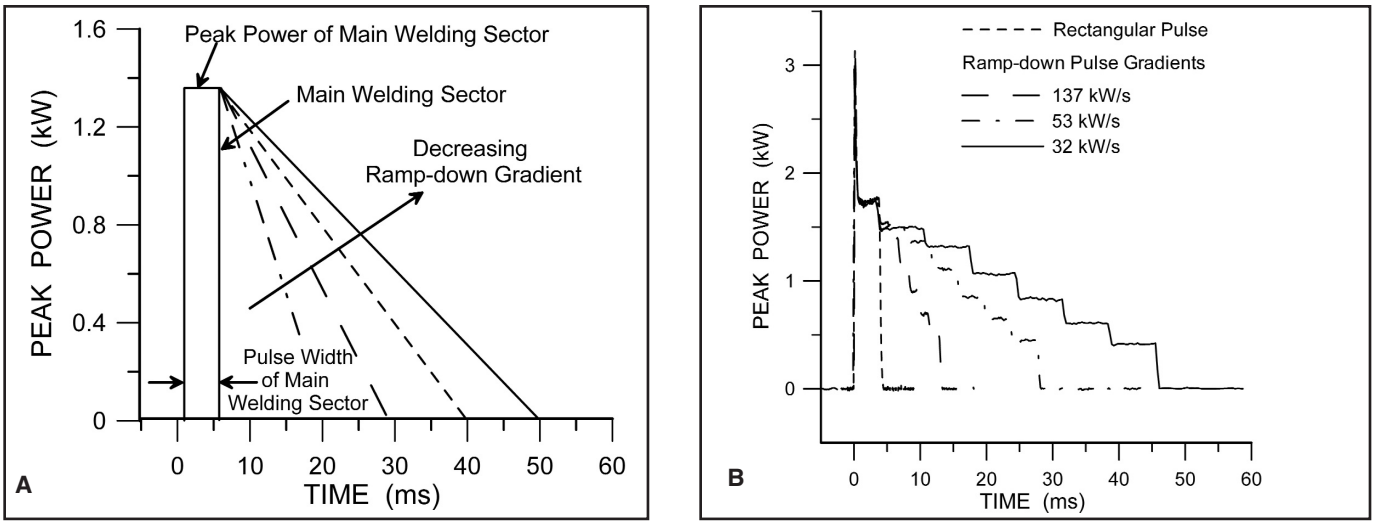

Fig. 4 — Ramp-down pulse shapes used the following: A — Schematic of waveform design; B — measured waveforms.

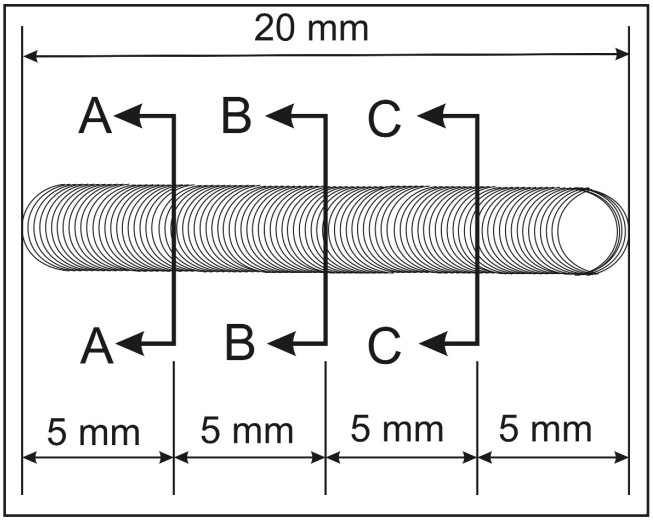

Fig. 5 — Schematic diagram showing the cross-sectioning positions used for metallographic examinations of the laser seam welds.

out of the filler metal alloy as shown in Fig. 1 or by making a special insert for the joint out of the filler metal alloy. However, filler metal alloys are not always available in the desired shapes and the extra parts and manufacturing steps required are time consuming and costly. Laser welded aluminum alloy hermetic packages have also been made successfully by Ni plating one or both aluminum parts prior to welding (Refs. 24, 25). The weld metal can be changed to a zero freezing range Al-Ni eutectic and solidification cracking avoided by plating an optimized thickness of Ni on the aluminum part prior to laser welding; however, this also requires an additional manufacturing step that can introduce other problems such as hydrogen porosity from the plating operation.

Table 2 — Laser Welding Process Parameters Used in This Study

Pulse frequency	5 Hz
Pulse width of main welding sector	4 ms
Peak power of main welding sector	1.26–2.21 kW
1/(ramp-down gradient)	0–19.7 ms/kW
Welding speed	0.3 mm/s
Focal position	0.0 mm
$1/e^2$ beam diameter	437 μm
Overlap rate	~87%
Argon shielding gas flow rate	0.24 L/s

Temporal pulse shaping has also been used to reduce or eliminate defects in welds made in various alloys using the pulsed Nd:YAG laser spot welding process (Refs. 26–30). A conventional pulsed laser welding beam pulse is simply on/off, i.e., it has a simple rectangular shape on a plot of laser beam power vs. time. However, temporal pulse shaping involves varying the laser beam power with time during the pulse in a predetermined manner. Temporal pulse shaping has been reported to be an effective method of modifying weld fusion area and penetration (Ref. 26) and reducing or eliminating a number of commonly observed defects in pulsed laser welds, such as porosity (Ref. 26) and solidification cracks (Refs. 28–30).

Matsunawa et al. (Refs. 28, 29) developed a laser pulse shape composed of two distinct pulses, the initial welding pulse followed by a second pulse a short time later. They found that using this pulse shape with a controlled decrease in beam power at the end of each pulse was beneficial in reducing cracking in A5083 aluminum and A7N01 stainless steel alloy welds. More recently, Michaud et al. (Ref. 27) developed an optimized ramp-down pulse shape that significantly reduced solidification cracking in individual spot welds in a pure binary Al-3.75 wt-% Cu alloy and produced crack-free seam welds. A thermal analysis of the optimized pulse shape on the pulsed laser welding conditions showed that solidification times and interface velocities were lower, and temperature gradients were higher during the solidification process (Ref. 31). Such conditions are known to have beneficial effects on the solidification microstructure and solidification cracking susceptibility (Refs. 9, 20, 21).

Temporal pulse shaping has the advantage over other methods of preventing various weld defects because it does not require the addition of a filler metal or use of extra manufacturing process steps such as plating. This simplifies the manufacturing process and makes it possible to fabricate the hermetic package using one single material, thereby improving the corrosion resistance of the package. However, most previous studies of the use of temporal pulse shaping during laser spot welding of aluminum alloys have been done using 2xxx and 5xxx series of aluminum alloys (Ref. 27). These alloys have lower solidification cracking indexes compared to 6061-T6 aluminum alloy (Refs. 8–13). The objective of the present study, therefore, was to study the effects of tem-

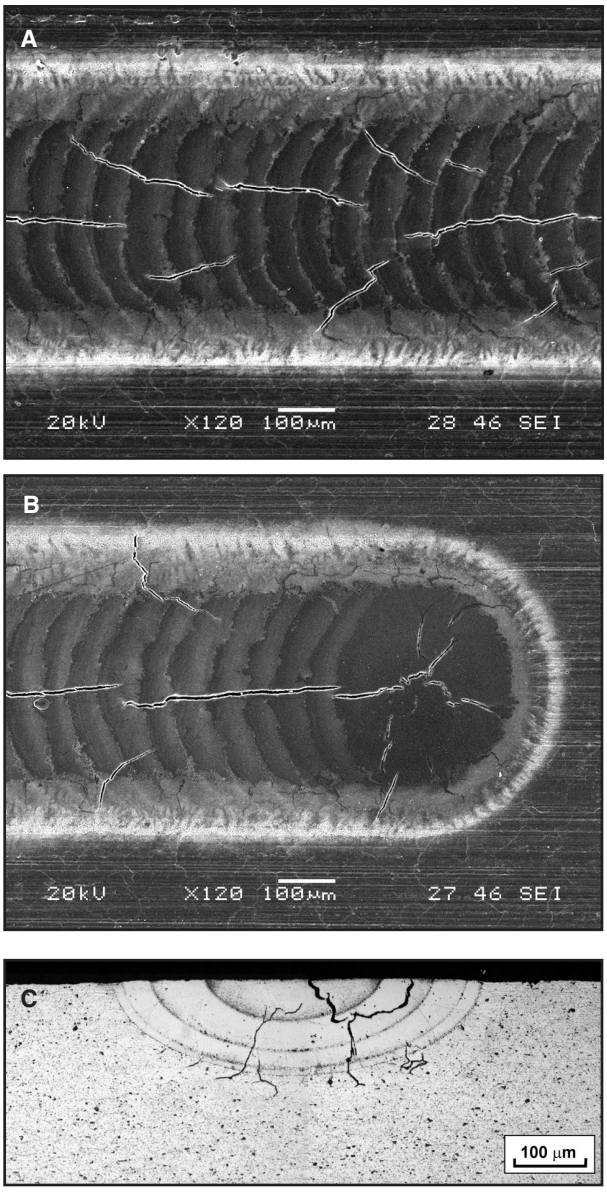

Fig. 6 — Severe solidification cracking in a weld made with a rectangular pulse shape with a peak power density of 11.5 GW/m^2: A — Weld bead during steady welding; B — end of weld bead with crater cracking; and C — transverse section.

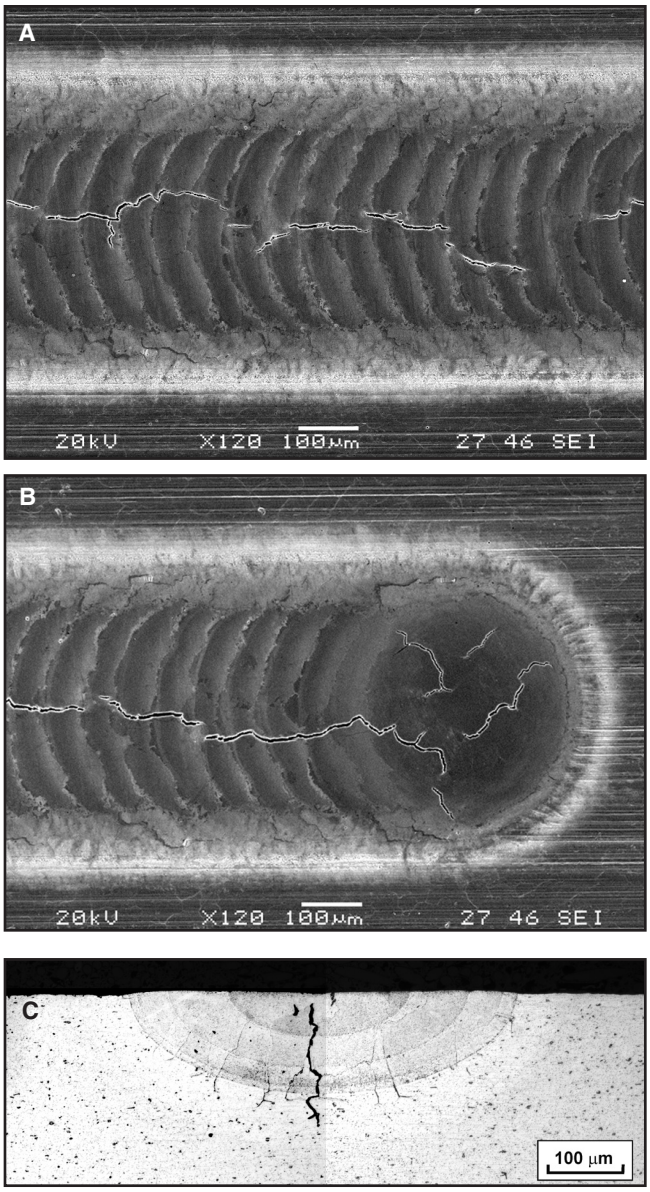

Fig. 7 — Intermittent solidification cracking in a weld made with a ramp-down pulse shape with main welding sector peak power density of 11.5 GW/m^2 and ramp-down gradient of 420 kW/s: A — Weld bead during steady welding; B — end of weld bead with crater cracking; and C — transverse section.

poral pulse shaping on solidification cracking susceptibility of pulsed laser seam welds on 6061-T6 aluminum. In this work, the influences of both ramp-down gradients and the peak power density of the main welding sector on characteristics such as total solidification crack length, solidification morphologies, and severity of microsegregation were examined.

Experimental Materials Apparatus and Methodology

The base metal used for this study was 6061-T6 aluminum with a nominal chemical composition as shown in Table 1 (Ref. 32). All samples were cut from 3.175-mm (0.125-in.) sheet into 50- × 50-mm coupons. Before welding, the as-received surface of each specimen was cleaned with acetone in an ultrasonic bath followed by a methanol rinse and air drying. The specimens were then clamped on the welding jig and laser seam welded.

All laser seam welds were made using a Lumonics JK702H pulsed Nd:YAG laser welding machine with a fiber-optic beam

Table 3 — EDS Measured Compositions (wt-%) at Locations ① to ⑥ in Fig. 15

Location	Mg	Si	Cr	Fe	Cu	Al
1	1.7	11.2	0.3	5.9	3.1	77.7
2	2.2	12.0	0.0	4.0	2.3	79.5
3	0.4	4.2	0.8	4.9	2.2	87.5
4	1.4	10.3	0.7	6.8	2.6	78.2
5	1.3	9.9	0.5	4.2	2.5	81.6
6	1.2	7.5	0.6	3.8	4.4	82.7
Base Metal	0.5	0.6	0.5	0.8	0.3	97.4

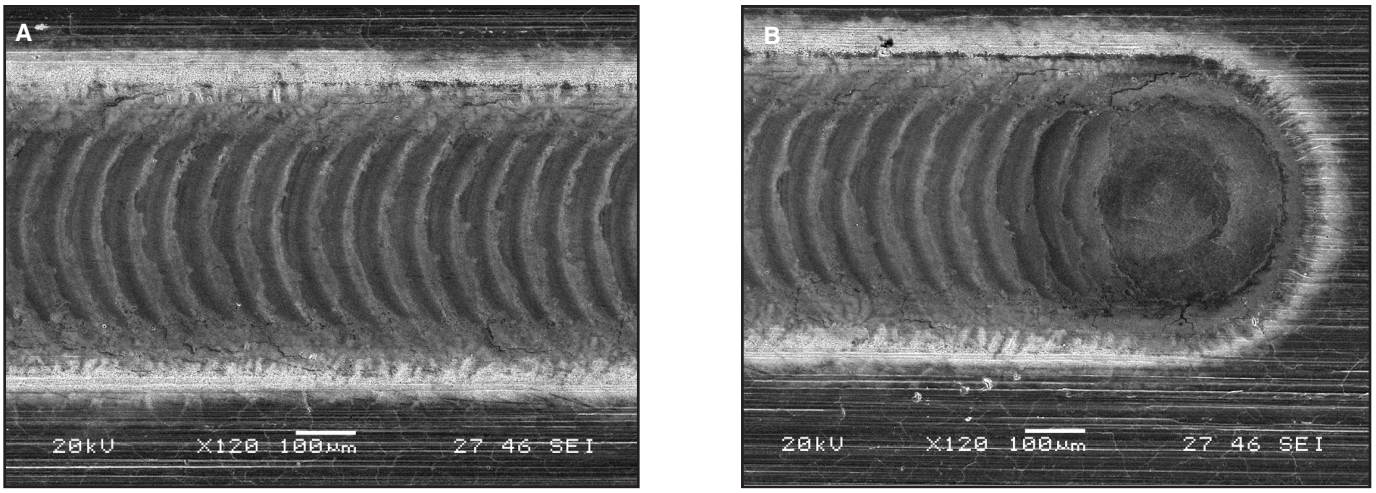

Fig. 8 — A sound weld made using a ramp-down pulse shape with main welding sector peak power density of 11.5 GW/m² and ramp-down gradient of 100 kW/s: A — Weld bead during steady welding; B — end of weld bead with crater area; and C — transverse section.

delivery system. A schematic diagram of the laser welding head and specimen clamping fixture is shown in Fig. 3. As indicated, the laser beam delivery head was tilted 15 deg from the normal to avoid backreflection of the laser beam. The Nd:YAG pulsed laser welding machine was capable of up to 350 W mean power, 0.5 to 20 ms pulse widths, maximum peak pulse power of up to 5000 W, and energy up to 55 J/pulse. The laser beam delivery system consisted of a 600-µm fiber-optic cable feeding into a beam delivery head with a 200-mm focal length collimator lens and a 120-mm final process lens. The intensity distribution of the laser beam at the focal plane was measured using a rotating-wire-type laser beam analyzer (Ref. 33) and a LeCroy 9410 digital oscilloscope. The beam profile was found to be well described by a Gaussian distribution with the $1/e^2$ beam diameter of 437 µm. The spot size of the pulsed laser beam was verified by the measurements of burn patterns produced in 25-µm-thick Kapton films using the technique developed by Wang et al. (Ref. 34). The internal laser energy meter was calibrated independently with an Ophir Optronics laser power/energy meter. Thus, the energy/pulse and peak power actually delivered to the surface of the material was well characterized. The nominal peak power density was calculated using the relation

$$P_D = \frac{4P_P}{\pi w_0^2} \times 1000 \qquad (1)$$

where P_D is the peak power density (GW/m²), P_P is the peak power (W), and w_0 is the $1/e^2$ beam diameter (µm).

The laser welding process parameters used in this study are listed in Table 2. All bead-on-plate seam welds were made with the laser beam focused on the surface of the specimen. The welding speed was kept at 0.3 mm/s and a pulse frequency of 5 Hz was used. This combination of welding speed and pulse frequency resulted in about 87% spot weld overlap rate, which is consistent with the normal requirement of 85–90% overlap to ensure the hermeticity of electronic packages (Ref. 35). A coaxial flow of argon shielding gas was supplied to the workpiece at a flow rate of 0.24 L/s through an 8-mm-diameter ceramic shielding gas nozzle set about 6 mm above the workpiece.

The temporal pulse shape technique used by Bransch et al. (Ref. 26) to change the pulse shape on the JK702H pulsed Nd:YAG laser welding machine when welding 304 stainless steel was used, i.e., each laser pulse was divided into sectors where the peak power and width of each sector were adjusted to obtain the desired temporal variation of power during a pulse. In the present study, an initial series of welds was produced using no pulse shaping, i.e., a normal rectangular or on/off shape laser pulse was used. However, following the arguments of Bransch et al. (Ref. 26), Michaud (Ref. 27), and Matsunawa and Katayama et al. (Refs. 28, 29), pulse shapes were then developed that involved a controlled rate of decrease of beam power after the initial rectangularly shaped welding pulse. Figure 4A shows a schematic of the idealized waveform design used in the present study for the ramp-down temporal shaping experiments. The initial rectangular portion of the pulse can be considered the "welding portion" of the pulse while the trailing ramp-down portion was considered the "solidification control portion" of the pulse. Both the peak power of the main welding sector and the ramp-down rate of the solidification portion of the pulse were adjusted to evaluate the effect of ramp-down gradient, R_g, and peak power density, P_d, on solidification cracking susceptibility. Weckman et al. (Ref. 36) found that pulsed laser weld dimensions in 1100 aluminum increased rapidly for the first 2 ms of laser pulse and changed little thereafter; therefore, a 4-ms main welding sector pulse width was used in the present study.

Figure 4B is an example of a series of measured ramp-down pulse shapes. The spike in power at the leading edge of the welding sector is characteristic of many solid-state pulsed laser welding machines and has been shown by Weckman et al. (Ref. 36), Bransch et al. (Ref. 26), and Michaud et al. (Ref. 27) to have no measurable effect on the final weld dimension or weld quality. Note that the actual ramp-down portion of the pulse is not linear, rather it consists of a series of individual pulse sectors of stepwise decreasing peak powers. As indicated in Table 2, laser seam welds were made using peak powers for the main welding sector ranging from 1.26 to 2.21 kW and $1/R_g$ values of 0 ms/kW (rectangular pulses) to 19.7 ms/kW (R_g = 50.8 kW/s).

Laser seam welds produced using a range of peak power densities of the main

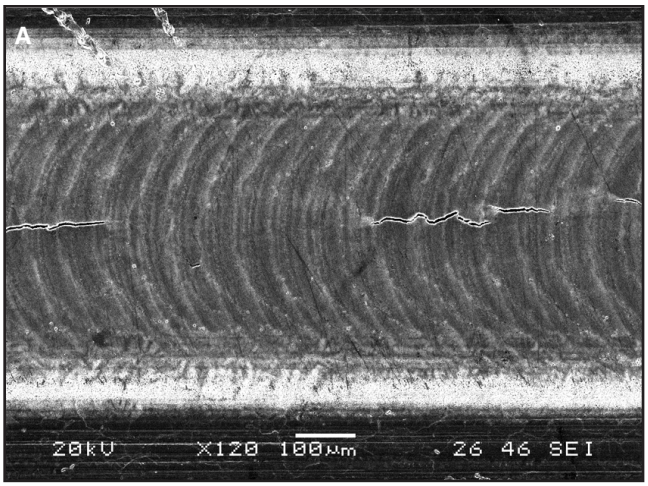

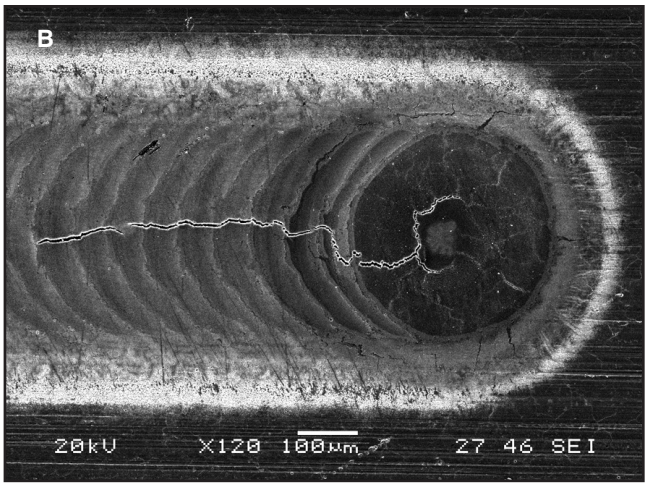

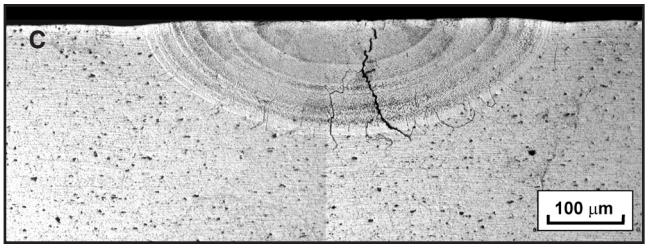

Fig. 9 — Intermittent solidification cracking in a weld made using a ramp-down pulse shape with main welding sector peak power density of 11.5 GW/m² and ramp-down gradient of 36 kW/s: A — weld bead during steady welding; B — end of weld bead with crater cracking; and C — transverse section.

welding sector and ramp-down gradients were transversely sectioned, as shown in Fig. 5. All sectioned samples were mounted, ground, and polished to a 0.06-μm colloidal silica finish. An optical metallographic microscope with image analysis system was employed to characterize the severity of cracking through measurements such as total crack length, number of cracks, and cracking area on polished, unetched specimens. The total crack length on transverse sections was found to have the least experimental scatter in data and most sensitivity to the effects of the various weld process parameters on cracking. Therefore, the total crack length on transverse sections was used to characterize the solidification cracking susceptibility of the laser welded 6061-T6 aluminum. Following crack length measurements, the specimens were etched using both Keller's reagent (Ref. 37) (5 mL HNO_3, 3 mL HCl, 2 mL HF, and 190 mL H_2O) and Graff and Sargent reagent (Ref. 37) (31 mL HNO_3, 1 mL HF, 6 g CrO_3, and 168 mL H_2O) in a two-step etching process to reveal the weld microstructure. Finally, surfaces of solidification cracks in welds were examined using a JEOL JSM-6460 scanning electron microscope (SEM) and composition measurements were made using energy dispersive spectroscopy (EDS). All SEM images were taken at 20 keV and a 13-mm working distance. The EDS measurements were conducted at 20 keV and a 20-mm working distance.

Results

Effect of Ramp-Down Gradients on Solidification Cracking Susceptibility

Figures 6–9 show bead-on-plate pulsed laser seam welds made on 6061-T6 alloy with a peak power density of the main welding sector of 11.5 GW/m² and various ramp-down gradients. Figure 6 shows a seam weld produced with a conventional rectangular pulse where welding was performed from left to right. In Fig. 6A, B, the original oxide layer was vaporized from the middle of the weld bead where the power density of the Gaussian distributed laser beam was greatest. However, the original surface oxide was not removed but remained floating on the weld pool surface toward the outside edges of the weld pool where the power density was much lower. The actual fusion zone width was greater than the width of ripples shown due to the much lower melting point of the aluminum base metal (925 K) relative to that of the aluminum oxide, Al_2O_3 (2373 K) on the specimen surface.

In Fig. 6A, B, severe solidification cracking initiated in one pulse and continued into subsequent spot welds following the local direction of solidification. Cieslak and Fuerschbach (Ref. 12) observed the same pattern of solidification cracking in pulsed Nd:YAG laser welds made in this same alloy. Significant crater cracking was evident in the crater at the end of the welds — Fig. 6B. Examination of the transverse sections such as shown in Fig. 6C revealed that severe solidification cracking had occurred in the weld metal and liquation cracking had occurred in the HAZ. The semicircular bands evident from the bottom to the top of the weld zone in Fig. 6C are the fusion boundaries of the sequential overlapping spot welds that form the seam weld.

As shown in Fig. 7, there was a reduction in severity of cracking observed when ramp-down pulse sectors were added to the initial rectangular pulse sector. In Fig. 7A, the solidification cracking was reduced to a single centerline crack that occurred intermittently along the seam weld. Notable crater cracking still existed in the crater at the end of the weld — Fig. 7B. The transverse section shown in Fig. 7C exhibited both solidification cracking in the weld metal and liquation cracking in the HAZ, but only down the centerline of the weld. In addition, some evidence of grain boundary liquation toward the sides away from the centerline was observed in both the weld metal and the HAZ.

As shown in Fig. 8, crack-free seam welds were achieved with further decrease of the ramp-down gradient to 100 kW/s. As may be seen in Fig. 8A, B, there was no evidence of solidification cracking on the surface of the weld bead during steady welding or in the crater area. The crack-like patterns in the crater in Fig. 8B were breaks in the oxide layer only. As shown in Fig. 8C, there were no cracks in the transverse sections, but there was some evidence of grain boundary liquation. This was confirmed by examination of the as-polished, unetched specimens as well as examination of the specimens using the SEM. A higher magnification photomicrograph of the interface region of one of these welds is shown in Fig. 13C.

Figure 9 shows a weld made with further reduction of the ramp-down gradient to 36 kW/s. As may be seen, intermittent

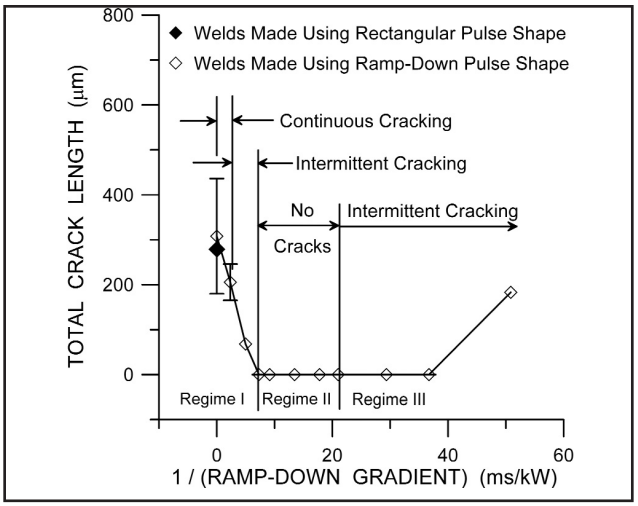

Fig. 10 — Total crack length vs. 1/(ramp-down gradient) for welds made with a welding sector peak power density of 8.1 GW/m².

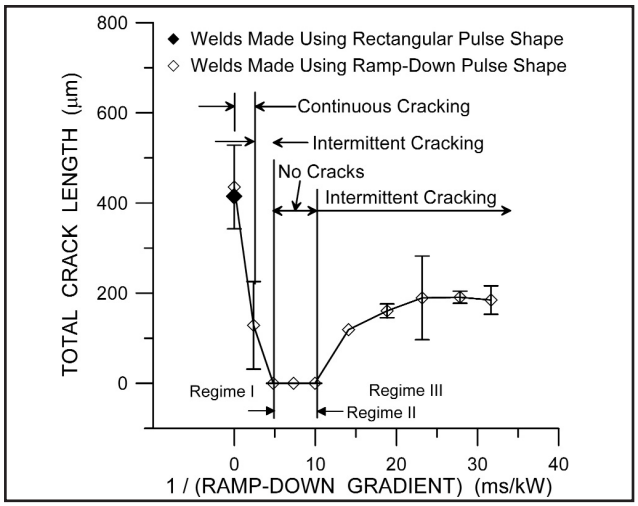

Fig. 11 — Total crack length vs. 1/(ramp-down gradient) for welds made with a welding sector peak power density of 11.5 GW/m².

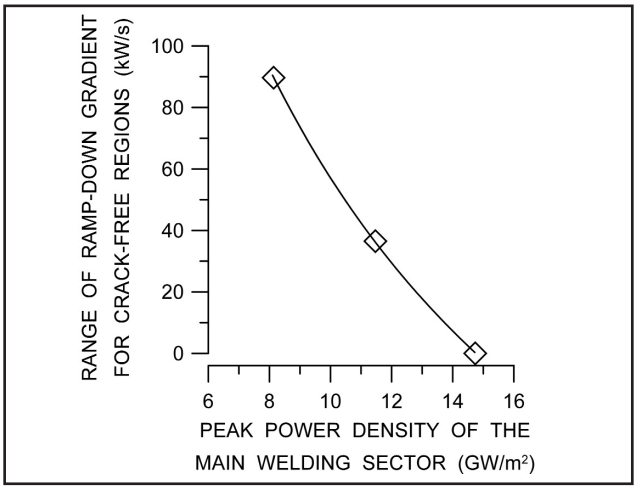

Fig. 12 — Range of ramp-down gradient for crack-free region vs. peak power density of the main welding sector.

solidification cracking was evident again. The intermittent solidification cracking occurred along the centerline of the weld bead (Fig. 9A) and there was crater cracking in the weld crater (Fig. 9B). Meanwhile, there was both solidification and liquation cracking located close to the centerline of the seam weld. As shown in Fig. 9C, some evidence of grain boundary liquation existed in both the weld metal and the HAZ.

Effects of Ramp-Down Gradient and Peak Power Density of Main Welding Sector on Solidification Cracking Susceptibility

Figure 10 shows a plot of total crack length as a function of $1/R_g$ for welds made with a peak power density of the main welding sector of 8.1 GW/m². Note that $1/R_g$ is used in these plots because the value of R_g for a rectangular pulse approaches infinity whereas $1/R_g$ is 0. There are three identifiable regimes for solidification cracking susceptibility evident in this plot. In Regime I, severe solidification cracking to intermittent cracking was observed in welds produced using rectangular pulses and relatively high ramp-down gradients such as those shown in Figs. 6 and 7. In Regime II, crack-free welds were produced using intermediate R_g values such as the weld shown in Fig. 8. Finally, in Regime III, intermittent cracking was exhibited again in welds produced using low R_g values such as the weld shown in Fig. 9. Note that the first two data points in this regime are zero only because, by chance, the three transverse sections were made in uncracked or sound portions of the welds with intermittent cracking evident on the weld bead surfaces.

The results in the first regime in Fig. 10, which showed decreasing cracking tendency with decreasing R_g (increasing $1/R_g$), is in good agreement with the results of the study by Michaud et al. (Ref. 27) on the use of temporal pulse shaping in laser welding of Al-Cu alloys and Matsunawa et al. (Refs. 28, 29) when working with 5083-O aluminum alloy and SUS 310S stainless steel. However, in Regime III, there was increasing solidification cracking susceptibility when R_g was further decreased. This behavior has not been previously reported.

As shown in Fig. 11, when the peak power density of the main welding sector was increased from 8.1 to 11.5 GW/m², the same trends in cracking behavior shown in Fig. 10 were observed; however, there was a noticeable decrease in the range of R_g values for the crack-free Regime II. Finally, crack-free welds could not be produced when the peak power density was further increased to 14.7 GW/m² and $1/R_g$ values from 0 to 18.0 ms/kW were used.

Figure 12 is a plot of the range of R_g values that could be used to produce crack-free welds vs. peak power density of the main welding sector. There was a clear trend that the range of R_g values that could be used to produce crack-free welds decreases with increasing peak power density of the main welding sector. These results indicated that the solidification cracking susceptibility was not only affected by R_g, but was also influenced by the peak power density of the main welding sector.

Metallographic Examination Results

Solidification cracking is known to be affected by alloy composition, solidification rate, and thermal gradient at the solid-liquid interface during weld metal solidification (Refs. 9, 20, 21). To help better understand the effect of R_g on solidification cracking susceptibility, it is useful to examine the effects of R_g on the solidification morphologies and microsegregation of alloy elements within the weld metal. For example, Fig. 13A shows the microstructure at the fusion boundary of a weld produced with the conventional rectangular pulse shape. There are fusion boundaries from three subsequent spot welds also evident in this photomicro-

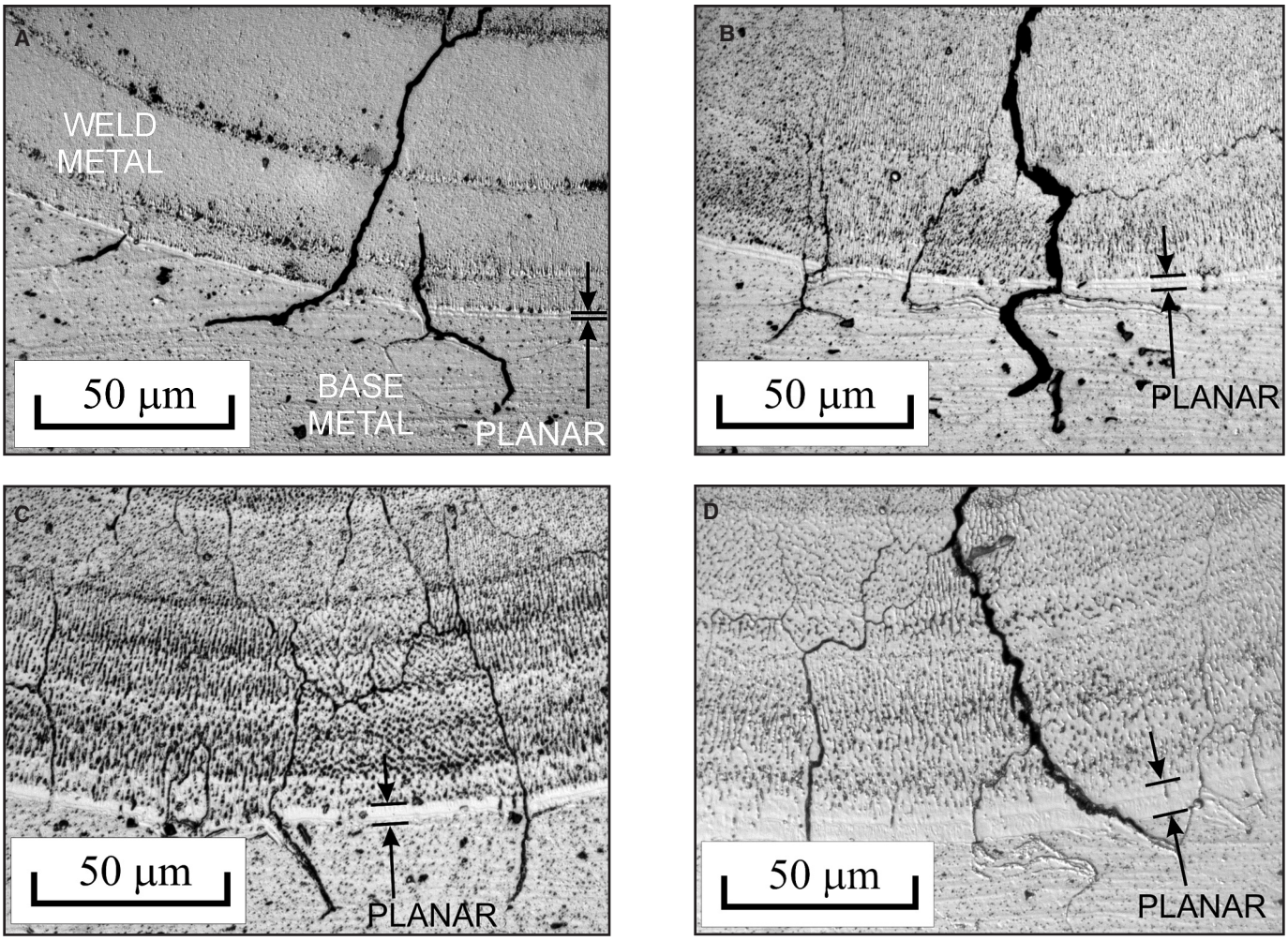

Fig. 13 — Effect of ramp-down gradient on solidification morphologies of welds made using a main welding sector peak power density of 11.4 GW/m² and the following: A — A rectangular pulse shape and pulses with ramp-down gradients of — B — 420 kW/s; C — 100 kW/s; and D — 36 kW/s.

graph. The solidification was initially planar over a narrow band at the fusion boundary adjacent to the base metal. This band was about 1.5 μm wide. Beyond this band of planar solidification, the interface broke down to a cellular-dendritic solidification structure that extended in a band that was about 5–8 μm wide — Fig. 13A. This transition of weld solidification microstructure can be explained in terms of the G/V ratio, where G is the temperature gradient in the liquid at the solid-liquid interface and V is the local growth rate (Refs. 9, 20, 21). Since V is expected to be initially small at the fusion boundary, G/V is large and planar growth takes place. However, as the laser spot welds begin to cool, V increases, G decreases (Ref. 31), and the growth morphology changes from planar to cellular-dendritic (Refs. 9, 20, 21). Planar growth was evident only when the weld bordered unmelted base metal. At fusion boundaries of subsequent spot welds in previously solidified weld metal, a planar growth region was less evident, although a band was often present — Fig. 13A. The dendritic structure was not visible beyond this point, suggesting a transition to a very fine solidification microstructure that was beyond the resolution of the optical microscope. There was severe solidification cracking in the weld metal and intergranular liquation cracking in the HAZ adjacent to the fusion boundary. There was also evidence of grain boundary liquation in the HAZ.

Welds produced with ramp-down pulse shapes exhibited very different microstructures. Figure 13B shows the microstructure of a weld produced with a peak power density of the main welding sector of 11.5 GW/m² and R_g of 420 kW/s ($1/R_g$ = 2.4 ms/kW). The microstructure at the very beginning of weld metal solidification was similar to that in the weld made with a rectangular pulse. However, the band of planar solidification adjacent to the fusion boundary was wider at about 3.5 μm. Beyond this band, the solidification morphology was cellular-dendritic — Fig. 13B. As solidification proceeded, the primary dendrite arm spacing (DAS) became finer until the cellular-dendrites reached the boundary of a subsequent spot weld. The solidification microstructure was coarser with larger primary DAS in this weld compared with that in the welds made with a rectangular pulse shape —Fig. 13A, B. The solidification cracking exhibited was less severe and was reduced to a single centerline crack that propagated along the grain boundary in the direction of solidification. The observed reduction of solidification cracking may be the result of improved ability of liquid metal to flow back to cellular-dendrites or dendrite roots at the final stage of weld metal solidification with larger DAS. Finally, as shown in Fig. 13B, there was some evidence of grain boundary liquation in the HAZ and continued solute segregation along the grain boundaries in the weld metal.

As shown in Fig. 13C, when the ramp-down gradient was further decreased to

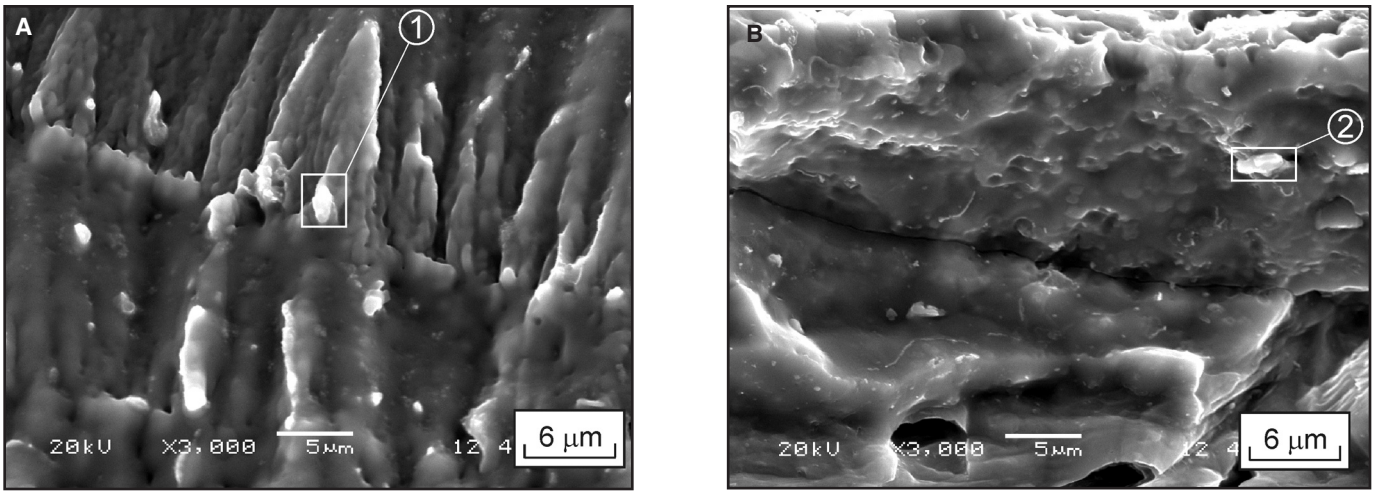

Fig. 14 — SEM photographs of crack surfaces in welds made using a rectangular pulse shape with peak power density of 11.5 GW/m²: A — Solidification crack in the weld metal; B — liquation crack in the HAZ adjacent to the fusion boundary.

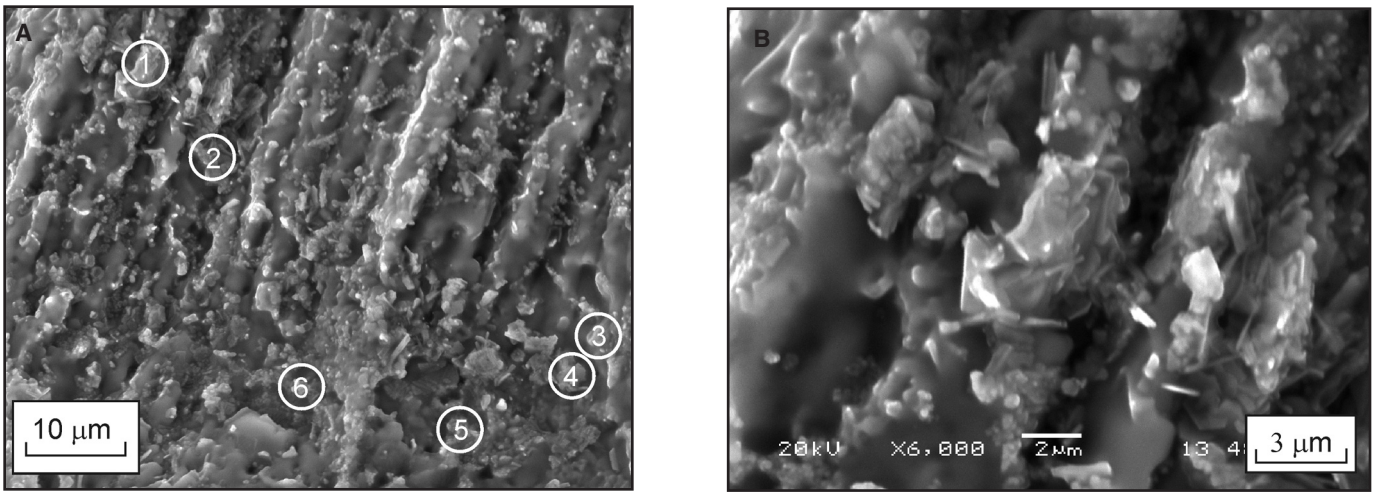

Fig. 15 — SEM photographs of crack surfaces in welds made using a ramp-down pulse shape with peak power density of the main welding sector of 11.5 GW/m² and ramp-down gradient of 3 kW/s: A — Overall crack surface; B — higher magnification for area of interest in ① in A.

100 kW/s ($1/R_g$ = 10 ms/kW), there was a notable increase of the width of the initial planar solidification band adjacent to the fusion boundary and the primary DAS in the weld metal. The width of the initial planar solidification band increased to about 5.5 μm. There was no solidification cracking or liquation cracking evident in this weld; however, there was noticeable evidence of grain boundary liquation in the HAZ and solute segregation along the weld metal grain boundaries.

As expected, the width of the initial planar solidification band increased when the ramp-down gradient was further decreased to 36 kW/s ($1/R_g$ = 28 ms/kW) — Fig. 13D. The width of the band of planar solidification in this weld is about 8.0 μm. Both solidification cracking and liquation were evident again. In the photomicrographs shown in Fig. 13A–D, the width of the initial planar growth band at the fusion boundary increased and the primary dendrite arm spacing in the remaining weld metal increased with decreased ramp-down gradient. This is indicative that lower solidification rates and higher thermal gradients exist during solidification of laser spot welds produced using decreasing ramp-down gradients in the laser pulse (Refs. 9, 20, 21).

SEM/EDS Investigation of Fracture Surface Compositions and Microsegregation

SEM/EDS analysis of the fracture surfaces of cracked welds made using a peak power density of the main welding sector at 11.5 GW/m² and a series of ramp-down gradients was performed to evaluate the morphology of the fracture surfaces, to obtain a measure of the element segregation that had taken place near the cracks, and to identify the chemical composition of second-phase particles observed on these crack surfaces. In order to provide a basis for comparison for the EDS results, freshly polished and cleaned samples of base metal were also analyzed.

Typical crack surfaces in the weld metal and the HAZ are shown in Fig. 14. Figure 14A shows well-developed cellular dendrites of the primary α phase. As may be seen at ①, some second-phase particles formed on the primary dendrite surfaces. The dendritic morphology of the crack surfaces further suggests that these cracks are solidification cracks. Figure 14B shows a liquation crack surface in the partially melted zone (PMZ) in the HAZ adjacent to the fusion boundary. There is evidence of solidification of the liquated thin film in the lower half of the image. The second-phase particle at ② is on the intergranular solidification crack in the weld metal adjacent to the fusion boundary.

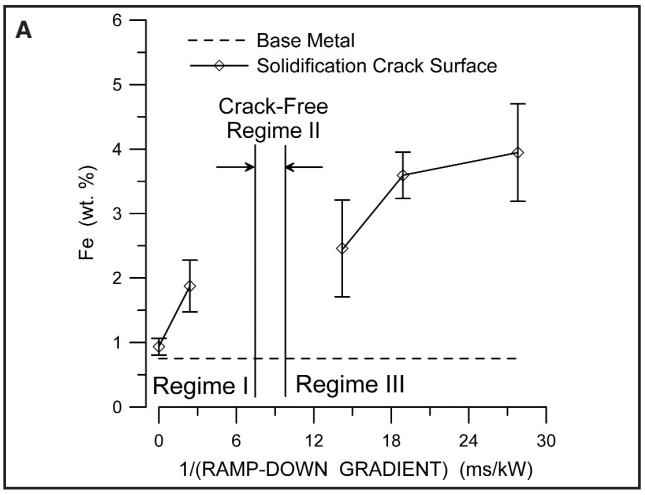

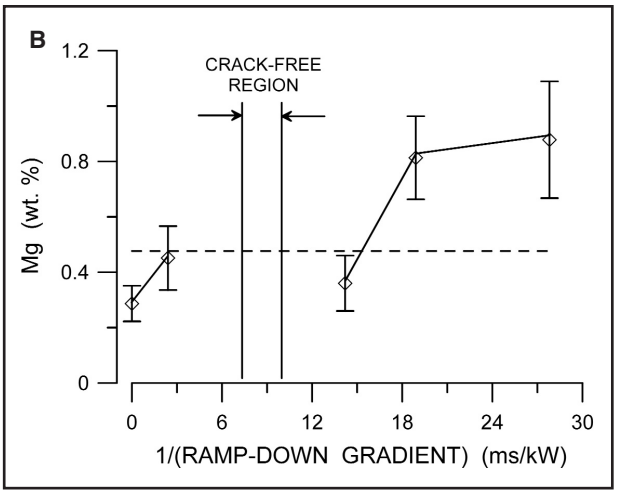

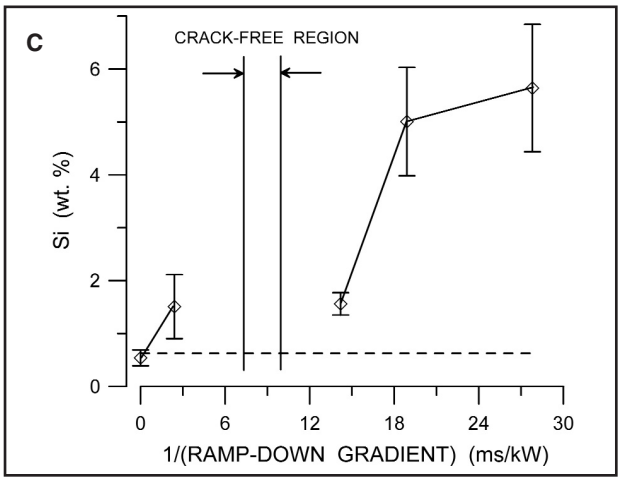

Fig. 16 — Weight-percent of alloy element detected on the solidification crack surface of a weld made with a main welding sector peak power density of 11.5 GW/m² vs. 1/(ramp-down gradient): A — Fe; B — Mg; C — Si.

SEM images of a solidification crack surface in a weld made using a ramp-down pulse shape with a peak power density of the main welding sector of 11.5 GW/m² and the slowest ramp-down gradient of 36 kW/s is shown in Fig. 15. Liquid that was drawn out into spikes or thin sheets by thermal strains during the last stages of weld metal solidification was also observed on crack surfaces — Fig. 15A. In addition, there were significantly more second-phase particles on the crack surface — Fig. 15A, B. As shown in Table 3, EDS analysis of these second-phase particles at locations ①–⑥ in Fig. 15A showed that they were Mg, Si, Fe, and/or Cu-rich phases.

EDS measurements of the overall chemical composition of the crack surfaces of welds with hot cracking were done at 500× magnification. This lower magnification was chosen as it provided higher accuracy and less scatter of the EDS results. It must be recognized that these EDS measurements cannot be expected to be quantitatively accurate as their resolution is poor when element concentrations are less than 1% because the energy peak associated with that element is very small and close to the normal background noise of the detector. Also, the electron beam excites not only the surface elements but a small volume of metal below the surface. Thus, the EDS measurement is an average measure of the composition in the excitation volume. If the surface film on the surface of the crack is thinner than the excitation volume, then EDS measurement of composition will not be quantitatively accurate. These measurements should, however, be qualitatively accurate.

As shown in Fig. 16, the average Fe, Mg, and Si concentrations on the crack surfaces increase slightly with increasing $1/R_g$ (decreasing ramp-down gradient) below the $1/R_g$ values that produce crack-free welds, i.e., in Regimes I and II. However, in Regime III, there is a dramatic increase in these solute concentrations on the crack surface when $1/R_g$ exceeds about 15 ms/kW. Most notably, the Fe concentration increased by about 4.5 times the nominal base metal composition, the Mg concentration increased by about 3 times the nominal base metal concentration, and the Si concentration increased by about 10 times the nominal base metal Si concentration when a pulse shape with a $1/R_g$ value of 28 kW/s was used compared with a rectangular pulse with the same peak power density. These increased solute concentrations can be expected to significantly lower the melting temperature and increase the freezing range of the liquid in the intergranular regions during solidification, thereby dramatically increasing the propensity for solidification cracking.

Discussion

Changes of laser welding process parameters can significantly influence the cooling rate, solid/liquid interface velocity, V, temperature gradient in the liquid, G, and microsegregation during weld metal solidification. These changes will in turn result in different solidification times, dendrite arm spacing, mushy zone width, dendrite growth rate, strain rate, cell or cellular dendrite length, and solidification temperature range. All of these factors ultimately affect the propensity for solidification cracking in 6061-T6 aluminum during solidification of laser spot welds.

Effects of Solidification Time

Solidification cracking is caused in part by difficulties in feeding liquid from the molten weld pool to the cellular-dendrite or dendrite roots during the solidification process and by tensile strains transverse to the solidification direction due to thermal contraction as the weld metal solidifies and cools (Refs. 9, 20, 21). If liquid can flow back freely between the dendrites as they are pulled away from each other during cooling, then voids created by the accumulation of thermomechanical strain from thermal contraction can be healed, thereby preventing solidification cracking. The thermal conditions present during rectangular and ramp-down pulse shapes can have a significant influence on these factors. Based on the work by Michaud et al. (Ref. 27) on Al-3.75 wt-% Cu for both a rectangular and an optimized ramp-down pulse shape, the solidification time for the ramp-down pulse shape was much longer than that of the rectangular pulse. Solidification cracking was not observed in this alloy when using the ramp-down pulse shape. Similar results were obtained by Matsunawa et al. (Refs. 28, 29) for an

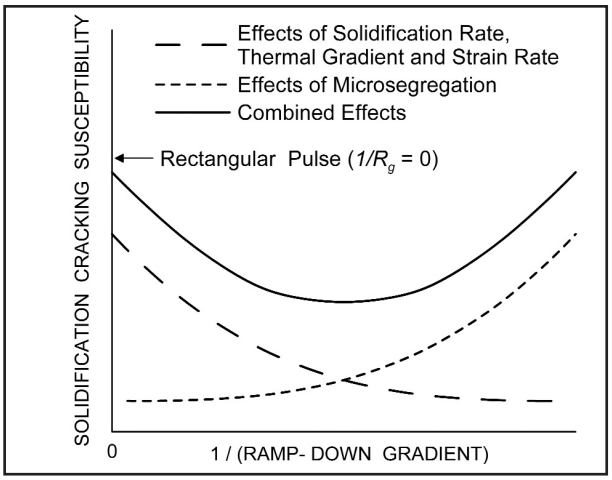

Fig. 17 — Schematic illustration of the factors that affect solidification cracking in pulsed laser welds in AA 6061 aluminum and the resultant solidification cracking susceptibility as a function of 1/(ramp-down gradient).

A5083-0 aluminum alloy using a pulse with a trailing pulse in comparison with a rectangular pulse shape. The longer solidification time experienced in welds produced with the ramp-down pulse shapes would allow more time for liquid to flow back to the cellular-dendrites or dendrite roots thereby reducing the solidification cracking susceptibility as was observed in Regimes I and II in Figs. 10 and 11; however, this does not explain why intermittent cracking returned with further decrease of the ramp-down rate in Regime III.

Effects of Interface Velocities during Solidification

From solidification theory, it is known that the interface velocity and temperature gradient at the solid-liquid interface during solidification affect the resulting solidification microstructure (Refs. 20, 21). A planar interface morphology will be formed at extremely high solidification rates where there is no time for diffusion in the liquid ahead of the interface or when the thermal gradient is high and the solidification velocity is low. At intermediate solidification rates and temperature gradients, a cellular-dendritic or dentric solidification morphology will be produced where the primary dendrite arm spacing, λ_1, can be calculated based on the equation proposed by Hunt (Ref. 38)

$$\lambda_1 = C\left(G^2 V\right)^{-\frac{1}{4}} \qquad (2)$$

where C is a material constant whose value is dependent on the alloy system, G is the temperature gradient, and V is the solid-liquid interface speed during solidification. For the ramp-down pulse shape, the interface velocities are lower than that for a rectangular pulse shape (Ref. 31), resulting in increased primary dendrite arm spacing and a coarser microstructure compared with the welds produced with a rectangular pulse shape. This is in qualitative agreement with the observed differences in weld metal microstructure of the welds produced using the rectangular and ramp-down pulse shapes shown in Fig. 13A–D. The coarser microstructure observed with the ramp-down pulse shape would lead to a larger cell or dendrite interstices and, thus, larger passages for the flow of liquid back to the cellular-dendrites or dendrite roots thereby resulting in reduced solidification cracking susceptibility. This is consistent with the observed decrease in crack length with decreasing ramp-down rates (increasing $1/R_g$) in Regimes I and II in Figs. 10 and 11; however, this also does not explain why intermittent cracking returned with further decrease of the ramp-down rate in Regime III.

Effects of Temperature Gradient on Cell or Cellular Dendrite Length

Based on a numerical thermal analysis by Michaud et al. (Ref. 31), the temperature gradients for ramped down pulse shapes are higher than those made by a rectangular pulse shape because heat is constantly being introduced into the surface of the weld pool during the ramp-down phase of the laser pulse and a higher thermal gradient is required to conduct this heat into the surrounding base metal. From solidification theory, the temperature gradient, G, directly influences the cell or cellular dendrite length, l_c, in the mushy zone. This is given approximately by (Refs. 20, 21)

$$l_c = \Delta T' / G = \frac{\left(T^* - T'_s\right)}{G} \qquad (3)$$

where $\Delta T'$ is the difference between the cell tip temperature, T^*, and the root temperature T'_s, and G is the temperature gradient. According to Equation 3, the increased thermal gradient at the interface with decreasing laser pulse ramp-down rate would result in shorter cells or cellular dendrites and therefore shorter feeding distance for liquid to flow back to the dendrite root. Consequently, cracks could be more easily healed by the liquid flowing back to the dendrite roots and the propensity for solidification cracking would be reduced. This reduced solidification cracking susceptibility with decreasing ramp-down gradient and higher thermal gradients during solidification is consistent with the results observed by Michaud et al. (Ref. 27) with a binary Al-3.75 wt-% Cu alloy and by Matsunawa et al. (Refs. 28, 29) with A5083-O aluminum and SUS 310S stainless steel. The data shown in Regions I and II in Figs. 10 and 11 are also consistent with these effects, that is, solidification cracking susceptibility in the 6061-T6 aluminum alloy decreased with decreasing ramp-down rate (increasing $1/R_g$). However, the reason for the increase in intermittent solidification cracking observed with further decrease of the ramp-down rate in Region III is not explained by Equation 3.

Effects of Cooling and Strain Rate during Weld Metal Solidification

The solidification rates and cooling rates of a spot weld produced using a rectangular laser pulse is greater than that of a ramp-down pulse shape (Ref. 31). This leads to higher deformation rates (strain rates) for welds produced using a rectangular pulse shape. According to a combination of Borland's generalized theory (Ref. 39) and the critical strain rate theory (Refs. 9, 11, 40, 41), an alloy at high temperature and most notably within the solidification temperature range is affected by a low-ductility brittle temperature range (BTR) near the solidus. In the BTR, cracking can occur in the material in which continuous liquid films separate grains or in which some solid-solid bridges exist between grains when localized tensile strains in the materials exceed its resistance to cracking or when the material is subjected to tensile strain at a rate faster than the critical tensile strain rate. For a normal rectangular pulse shape, the higher cooling rate and higher interface velocity will lead to higher strain rates as the metal cools through the BTR. Alternatively, the lower cooling and strain rates present when using the ramp-down pulse shape will decrease the tendency for cracking as the material cools through the BTR. The experimental results in Regimes I and II in Figs. 10 and 11 are consistent with this theory for solidification cracking susceptibility; however, the reason for the return of intermittent cracking with further decrease of the ramp-down rate in Regime III remains unexplained.

Microsegregation

Hot cracking of aluminum alloy welds is influenced metallurgically by the freezing

temperature range of the dendrites during nonequilibrium solidification and the type and amount of liquid available at the root of the dendrites during solidification. These are affected mainly by the weld metal composition and microsegregation that occurs during solidification (Refs. 17–19, 22, 41). Microsegregation, in turn, can be affected by the cooling rate during solidification. The cooling rate during solidification of a laser spot weld made using a ramp-down pulse shape is lower than one made with a rectangular pulse shape, so there is more time available for microsegregation to take place in the interdentritic and intergranular regions of the microstructure. In most cases, this will result in a solute-rich liquid film in the interdendritic and intergranular regions that has a much lower melting temperature and greater freezing range than the base material. This low-melting-point liquid film is unable to resist the thermomechanical contraction strains that take place during cooling, and voids and solidification cracking will occur. Low ramp-down gradients may also provide enough time for low-melting-point eutectics to form at cell or grain boundaries. Low-melting-point eutectics can be formed in 6xxx series AP-Mg-Si alloy systems such as Al-Mg_2Si, Al-Si, Al-Mg_2Si-Fe-$Mg_3Si_6Al_8$-Si, Al-Mg_2Si $(CrFe)_4Si_4Al_{13}$-Si, Al-$CuAl_2$-Mg_2Si, Al $Cu_2Mg_8Si_6Al_5$-$CuAl_2$-Si, etc. The melting temperatures of these eutectics range from 787 to 868 K (Ref. 42), which are much lower than the liquidus temperature of 6061-T6 (925 K) (Refs. 32, 42). Hatch (Ref. 43) has reported that coarse Mg_2Si was present in 6061 aluminum and a Al-Mg_2Si eutectic could be formed with a eutectic temperature of 868 K in this alloy. Also, Huang and Kou (Ref. 44) observed Si-, Fe-, and Cr-rich particles in the base metal of 6061 aluminum and segregation of Si up to 20 wt-% and Mg up to 10 wt-% at the grain boundaries in the partially melted zone (PMZ) of gas tungsten arc welded 6061-T6 aluminum alloy in addition to Fe-, Si-, Cr-, and Mn-rich particles in the PMZ. The formation of such eutectics and solute-rich liquid films will increase the freezing range of the alloy and increase the susceptibility of this alloy to solidification cracking.

As shown in Fig. 16, the severity of Fe, Mg, and Si microsegregation on the solidification crack surface increased with a decrease of the ramp-down gradient especially in Regime III where the ramp-down gradient used was lowest (highest $1/R_g$). In addition, solidification cracking susceptibility increased in Regime III as the ramp-down gradient was decreased (see Figs. 10 and 11). This suggests that reappearance of solidification cracking in Regime III may be caused by severe interdendritic and intergranular microsegregation and the formation of low-melting-point liquid films that occurred when the ramp-down gradients were reduced to low levels and solidification times were increased.

Summary of the Effects of Temporal Pulse Shaping on Solidification Cracking Susceptibility

Based on the previous results and discussions, it is clear that the effects of longer solidification time, larger dendrite arm spacing, narrower mushy zone, and smaller strain rate during welding metal solidification would benefit the reduction and elimination of solidification cracking when decreasing the ramp-down gradient. However, longer cells and more severe microsegregation would cause feeding problems for the remaining liquid metal to flow back to the dendrite roots and widen the solidification temperature range, resulting in increased solidification cracking tendency, when decreasing the ramp-down rate further. Figure 17 illustrates the combined effects of the above-mentioned factors as a function of the ramp-down gradient. The resultant solidification cracking susceptibility would follow the trends of decreasing to increasing cracking tendency when decreasing the ramp-down gradient (increasing $1/R_g$) as was observed in Figs. 10 and 11. As shown in Fig. 17, a crack-free or less severe cracking region may be reached when the cumulative influences of both effects are minimized.

Conclusions

In the present study, the effects of temporal pulse shaping, specifically the effects of ramp-down gradient and peak power density of the main welding sector, on solidification cracking susceptibility of pulsed Nd:YAG laser beam welds made in 6061-T6 aluminum alloy were examined. The results showed that it was possible to eliminate solidification cracking in 6061-T6 pulsed Nd:YAG laser seam welds using temporal pulse shaping. The solidification cracking susceptibility was found to decrease with decreasing ramp-down gradient. A limited, intermediate range of ramp-down gradients resulted in sound, crack-free welds; however, intermittent solidification cracking occurred again when the gradient was further decreased.

There were three identifiable regimes of solidification cracking susceptibility with decreasing ramp-down gradients for welds made with the peak power densities of the main welding sector less than 11.5 GW/m^2. Regime I showed decreasing cracking tendency with decreasing ramp-down gradients. This is in good agreement with previous studies of the use of temporal pulse shaping during pulsed laser welding of Al-Cu and Al-Mg alloys. It is thought that cracking in the laser spot welded 6061-T6 was reduced with decreasing ramp-down gradient in Regime I because of the beneficial effects of longer solidification time, larger dendrite arm spacing, narrower mushy zone, and smaller strain rate during weld metal solidification. Regime II was the crack-free region. However, intermittent solidification cracking was exhibited again in Regime III, in which the solidification cracking susceptibility increased with a further decrease of the ramp-down gradients. In this case, it was thought that longer cells and more severe microsegregation caused feeding problems for the remaining liquid metal to flow back to the dendrite roots and widened the solidification temperature range, thus resulting in increased solidification cracking tendency in Regime III when the ramp-down rate is decreased further beyond that used in Regime II.

The crack-free range of ramp-down gradients that produced welds decreased when the peak power density of the main welding sector was increased. Crack-free welds could not be produced when the peak welding power density was greater than 11 GW/m^2. Thus, the solidification cracking susceptibility was not only affected by the ramp-down gradient, but was also influenced by the peak power density of the main welding sector.

The weld metal solidification structures for welds made using a ramp-down pulse shape were different from those made using a rectangular pulse. The width of the initial planar grain growth layer at the fusion boundaries and cell spacing increased with decreasing ramp-down gradient in the laser pulses. Following the initial planar solidification, there was a transition to cellular and then cellular-dendritic solidification. The typical solidification crack surfaces in the weld metal revealed well-developed cellular dendrites of the primary phase. Some Cu-, Fe-, Mg-, and/or Si-rich second phases formed on the primary dendrite surfaces. EDS measurements of the overall chemical composition of the solidification crack surfaces of welds showed a clear trend that Cu, Fe, Mg, and Si microsegregation to the grain boundaries increased with decreasing ramp-down gradients. This increased microsegregation was thought to be the cause of the return of intermittent solidification cracking in Regime III where low ramp-down gradients were used.

In summary, temporal pulse shaping can be used to affect the solidification time, the dendrite arm spacing, the size of the mushy zone, the strain rate, and the severity of interdendritic and intergranu-

lar microsegregation of alloying elements during weld metal solidification. These in turn influence the resultant solidification cracking susceptibility. Crack-free pulsed laser seam welds could be made in 6061-T6 aluminum alloy by using a limited range of intermediate ramp-down gradients where both the positive and the detrimental effects of laser pulse ramp-down rate were at an optimum level.

Acknowledgments

This work was supported by the Ontario Research and Development Challenge Fund (ORDCF) Project "Centre for Automotive Materials and Manufacturing (CAMM)-Waterloo."

References

1. Johnson, B. C. 1991. *Electronic Materials Handbook,* Vol. 1, Packaging, ed. M. L. Minges. Materials Park, Ohio: ASM International. pp. 397–503.

2. Wong, C. P., and Fang, T. 2001. *Fundamentals of Microsystems Packaging*, ed. R. R. Tummala. New York, N.Y.: McGraw-Hill. pp. 580–610.

3. Sampson, R. N., and Mattox, D. M. 1991. Materials for electronic packaging. *Electronic Packaging and Interconnection Handbook*, ed. C. A. Harper. New York, N.Y.: McGraw-Hill, Inc. pp. 1.1–1.73.

4. Khanna, P. K., Bhatnagar, S. K., and Gust, W. 1999. Analysis of packaging and sealing techniques for microelectronic modules and recent advances. *Microelectronics Intl.* 16(2): 8–12.

5. Rossi, D. 1986. Choosing the proper device sealing technique. *Electronic Packaging & Production* 26(2): 188–194.

6. Harris, D. B. 1991. Electronic assemblies. *Handbook of Electronic Package Design*, ed. M. Pecht. New York, N.Y.: Marcel Dekker, Inc. pp. 153–238.

7. Steen, W. M. 1991. *Laser Materials Processing*. New York, N.Y.: Springer-Verlag.

8. *Metals Handbook,* Vol. 6*, Welding, Brazing, and Soldering*, 10th ed. 1993. Materials Park, Ohio: ASM International.

9. Kou, S. 2003. *Welding Metallurgy*, 2nd ed. Hoboken, N.J.: Wiley-Interscience, John Wiley & Sons.

10. Arata, Y., Matsuda, F., Nakata, K., and Sasaki, I. 1976. Solidification crack susceptibility of aluminum alloy weld metal (report I). *Trans. JWRI* 5(2): 53–67.

11. Arata, Y., Matsuda, F., Nakata, K., and Shinpzaki, K. 1977. Solidification crack susceptibility of aluminum alloy weld metal (report II). *Trans. JWRI* 6(1): 91–104.

12. Cieslak, M. J., and Fuerschbach, P. W. 1988. On the weldability, composition, and hardness of pulsed and continuous Nd:YAG laser welds in aluminum Alloys 6061, 5456, and 5086. *Metall. Trans. B* 19B: 319–329.

13. Matsuda, F., and Nakata, K. 1995. Evaluation of ductility characteristics and cracking susceptibility of Al alloys during welding. *Trans. JWRI* 24(1): 83–94.

14. Zhao, H., While, D. R., and DebRoy, T. 1999. Current issues and problems in laser welding of automotive aluminum alloys. *Int. Mater. Reviews* 44(6): 238–266.

15. Cam, G., and Kocak, M. 1998. Progress in joining of advanced materials. *Int. Mater. Rev.* 43(1): 1–44.

16. Ion, J. C. 2000. Laser beam welding of wrought aluminum alloys. *Sci. Technol. Weld. Join.* 5(5): 265–276.

17. David, S. A., and Vitek, J. M. 1989. Correlation between solidification parameters and weld microstructures. *Int. Mater. Reviews* 34(5): 213–245.

18. Katayama, S. 2000. Solidification phenomena of weld metals: Solidification cracking mechanism and cracking susceptibility (3rd report). *J. Light Metal Welding & Construction* 38(9): 13–23 (also 2001, *Welding Int'l.*, 15(8): 627–636).

19. Kou, S. 2003. Solidification and liquation cracking issues in welding. *JOM* 55(6): 37–42.

20. Flemings, M. C. 1974. *Solidification Processing*. New York, N.Y.: McGraw-Hill Inc.

21. Kurz, W., and Fisher, D. J. 1992. *Fundamentals of Solidification*, 3rd ed., Aedermannsdorf, Switzerland: Trans Tech Publications Ltd.

22. Dudas, J. H., and Collins, F. R. 1966. Preventing weld cracks in high-strength aluminum alloys. *Welding Journal* 45(6): 241-s to 249-s.

23. Iikawa, T., Sakai, T., Okamoto, S., Natori, K., and Nagai, T. 1986. Aluminum alloy package for microwave amplifier. *IEEE Trans., Components, Hybrids, and Manufacturing Technologies* CHMT-9 (4): 513–517.

24. Sakai, T., Okamoto, S., Iikawa, T., Sato, T., and Henmi, Z. 1987. A new hermetic sealing technique for aluminum packaging. *IEEE Trans., Components, Hybrids, and Manufacturing Technologies* CHMT-10 (3): 433–436.

25. Biro, E., Zhou, Y., Weckman, D. C., and Ely, K. J. 2001. The effects of Ni and Au/Ni platings on laser welding of thin sheets. *J. Laser Appl.* 13(3): 96–104.

26. Bransch, H. N., Weckman, D. C., and Kerr, H. W. 1994. Effects of pulse shaping on Nd:YAG spot welds in austenitic stainless steel. *Welding Journal* 73(3): 141-s to 151-s.

27. Michaud, E. J., Kerr, H. W., and Weckman, D. C. 1995. Temporal pulse shaping and solidification cracking in laser welding Al-Cu alloys. *Proc. 4th Int'l. Conf. Trends in Welding Research*, eds. H. B. Smart, J. A. Johnson, and S. A. David, Materials Park, Ohio: ASM International. pp. 153–158.

28. Matsunawa, A., Mizutani, M., and Katayama, S. 1996. Mathematical modeling of fusion and solidification in laser welding and evaluation of hot cracking susceptibility. *Trans. JWRI* 25(2): 161–169.

29. Katayama, S., Mizutani, M., and Matsunawa, A. 1997. Modelling of melting and solidification behaviour during laser spot welding. *Sci. Technol. Weld. Join.* 2(1): 1–9.

30. Kim, H. B., and Lee, C. H. 1999. Effect of Nd:YAG laser pulse shape on welding characteristics of STS 310S stainless steel. *Sci. Technol. Weld. Join.* 4(1): 51–57.

31. Michaud, E. J., Weckman, D. C., and Kerr, H. W. 1994. Effects of pulse shape on predicted thermomechanical strains in Nd:YAG laser welded aluminum. *Proc. ICALEO'94, LIA* Vol. 79, eds. T. D. McCay, A. Matsunawa, and H. Hügel. Orlando, Fla.: Laser Inst. America. pp. 461–470.

32. *Metals Handbook,* Vol. 2*, Properties and Selection: Nonferrous Alloys and Special-Purpose Materials*, 10th ed. 1990. Materials Park, Ohio: ASM International.

33. Hirak, D. M., Weckman, D. C., and Kerr, H. W. 1994. Measuring the spatial intensity distribution of high-power focused laser beams using a rotating-wire type laser beam analyzer. *Meas. Sci. Technol.* 5: 1513–1532.

34. Wang, Z. Y., Liu, J. T., Hirak, D. M., Weckman, D. C., and Kerr, H. W. 1993. Determining the spot size and Gaussian distribution coefficient of pulsed laser beams using Kapton films. *J. Laser Appl.* 5(1): 5–12.

35. Kugler, T. R. 2001. Nd:YAG pulsed-seam welding. *LIA Handbook of Laser Materials Processing*, eds. J. F. Ready and D. F. Farson. Orlando, Fla.: Laser Inst. America. pp. 339–342.

36. Weckman, D. C., Liu, J. T., and Kerr, H. W. 1997. The effect of process variables on pulsed Nd:YAG laser spot welds: Part II. AA 1100 aluminum and comparison to AISI 409 stainless steel. *Metall. Trans. B* 28B: 687–700.

37. Vander Voort, G. F. 1999. *Metallography, Principles and Practice.* Materials Park, Ohio: ASM International. pp. 165–199 and 610–614.

38. Hunt, J. D. 1979. Cellular and primary dendrite spacings. *Proc. Solidification and Casting of Metals*. London, UK: The Metal Soc. pp. 3–9.

39. Borland, J. C. 1960. Generalized theory of super-solidus cracking in welds (and casting). *Br. Welding J.* 7(8): 508–512.

40. Matsuda, F., and Nakata, K. 1995. Evaluation of ductility characteristics and cracking susceptibility of Al alloys during welding. *Trans. JWRI* 24(1): 83–94.

41. Katayama, S. 2000. Solidification phenomena of weld metals (2nd report): solidification theory, solute redistribution and microsegregation behaviour. *J. Light Metal Welding Construction* 38(4): 12–24 (also *Welding Int'l.*, 2001, 14(12): 952–963).

42. Mondolfo, L. F. 1976. *Aluminum Alloys: Structure and Properties*. London, UK.: Butterworth & Co. Ltd. pp. 759–805.

43. Hatch, J. E. 1984. *Aluminum: Properties and Physical Metallurgy*. Materials Park, Ohio: ASM International.

44. Huang, C., and Kou, S. 2002. Liquation mechanism in multicomponent aluminum alloys during welding. *Welding Journal* 81(10): 211-s to 222-s.